23. K. Gudmundsdottir, A. Ashworth, *Oncogene* **25**, 5864 (2006).
24. V. Joukov *et al*., *Cell* **127**, 539 (2006).
25. L. C. Gowen, B. L. Johnson, A. M. Latour, K. K. Sulik, B. H. Koller, *Nat. Genet.* **12**, 191 (1996).
26. D. M. Eccles, S. Barker, D. T. Pilz, C. Kennedy, *J. Med. Genet.* **40**, 24e (2003).
27. D. Eccles, D. Bunyan, S. Barker, B. Castle, *J. Med. Genet.* **42**, e42 (2005).
28. Y. Houvras *et al*., *J. Biol. Chem.* **275**, 36230 (2000).
29. B. Gao *et al*., *FEBS Lett.* **488**, 179 (2001).
30. A. Dubrovska *et al*., *Oncogene* **24**, 2289 (2005).
31. L. Garcia-Campmany, E. Marti, *Development* **134**, 65 (2007).
32. E. E. Govek, S. E. Newey, L. Van Aelst, *Genes Dev.* **19**, 1 (2005).
33. N. E. Ziv, S. J. Smith, *Neuron* **17**, 91 (1996).
34. D. R. Alessi *et al*., *EMBO J.* **15**, 6541 (1996).
35. D. Lang, S. K. Powell, R. S. Plummer, K. P. Young, B. A. Ruggeri, *Biochem. Pharmacol.* **73**, 1 (2007).
36. Q. Yan *et al*., *J. Biol. Chem.* **282**, 13954 (2007).
37. S. S. Shen-Orr, R. Milo, S. Mangan, U. Alon, *Nat. Genet.* **31**, 64 (2002).
38. T. Miralem, H. K. Avraham, *Mol. Cell. Biol.* **23**, 579 (2003).
39. This research is supported by the NIH grants GM54508 and GM072853 and Systems Biology Center grant P50-071558. Confocal laser scanning microscopy was performed at the Mount Sinai School of Medicine–Microscopy Shared Resource Facility, supported with funding from NIH–National Cancer Institute shared resources grant 5R24 CA095823-04, NSF Major Research Instrumentation grant DBI-9724504, and NIH shared instrumentation grant 1 S10 RR0 9145-01. We thank C. Karan and R. Realubit and the Rockefeller High Throughput Screening Resource Center for expert technical assistance in hippocampal neuron imaging and neurite outgrowth analysis. We thank E. Reddy for the c-Myb expression construct and members of the Iyengar laboratory for helpful discussions. K.D.B is supported by an individual American Cancer Society Spirit of Birmingham and Johnson Memorial Postdoctoral Fellowship Award and was supported by NIH grant T32 CA88796. Author contributions are described in the supporting online material.

Supporting Online Material
www.sciencemag.org/cgi/content/full/320/5878/903/DC1
Materials and Methods
Figs. S1 to S13
Tables S1 to S6
References

6 November 2007; accepted 5 March 2008
10.1126/science.1152662

Turbulence and Magnetic Fields in the Large-Scale Structure of the Universe

Dongsu Ryu,[1]* Hyesung Kang,[2] Jungyeon Cho,[1] Santabrata Das[3]

The nature and origin of turbulence and magnetic fields in the intergalactic space are important problems that are yet to be understood. We propose a scenario in which turbulent-flow motions are induced via the cascade of the vorticity generated at cosmological shocks during the formation of the large-scale structure. The turbulence in turn amplifies weak seed magnetic fields of any origin. Supercomputer simulations show that the turbulence is subsonic inside clusters and groups of galaxies, whereas it is transonic or mildly supersonic in filaments. Based on a turbulence dynamo model, we then estimated that the average magnetic field strength would be a few microgauss (μG) inside clusters and groups, approximately 0.1 μG around clusters and groups, and approximately 10 nanogauss in filaments. Our model presents a physical mechanism that transfers the gravitational energy to the turbulence and magnetic field energies in the large-scale structure of the universe.

There is growing evidence that the intergalactic medium (IGM) is permeated with magnetic fields and is in a state of turbulence, similar to the interstellar medium within galaxies. Magnetic fields in the intracluster medium (ICM) have been measured with a variety of techniques, including observations of diffuse synchrotron emission from radio halos, inverse-Compton scattered cosmic background radiation in extreme ultraviolet and hard x-ray radiation, and Faraday rotation measure (RM). The inferred strength of the magnetic field is on the order of 1 μG (*1*–*3*). In the IGM outside of clusters, an upper limit of ~0.1 μG has been placed on the magnetic field strength of filaments, based on the observed limit of the RMs of background quasars (*4*, *5*).

So far, signatures of turbulence have been observed only in the ICM. The analysis of the gas pressure maps of the Coma cluster revealed that pressure fluctuations are consistent with Kolmogoroff turbulence, and turbulence is likely to be subsonic with $\varepsilon_{turb} \gtrsim 0.1\ \varepsilon_{th}$, where ε_{turb} and ε_{th} are the turbulence and thermal energy densities, respectively (*6*). These results agree with predictions of numerical simulations of large-scale structure (LSS) formation (*7*, *8*). Turbulence in the ICM also has been studied in RM maps of a few clusters (*9*, *10*).

It has been suggested that cosmological shocks with Mach numbers up to ~10^4 and speeds up to a few thousand kilometers per second exist in the IGM (*11*–*13*). Such shocks result from the supersonic flow motions that are induced by the hierarchical formation of LSS in the universe. They are collisionless shocks, which form in a tenuous plasma via collective electromagnetic interactions between particles and electromagnetic fields (*14*). The gravitational energy released during the structure formation is transferred by these shocks to the IGM plasma in several different forms: in addition to the gas entropy, cosmic rays are produced via diffusive shock acceleration (*15*, *16*), magnetic fields are generated via the Biermann battery mechanism (*7*, *17*) and Weibel instability (*18*, *19*), and vorticity is generated at curved shocks (*20*, *21*).

In astrophysical plasmas in which charged particles are coupled to magnetic fields, turbulent-flow motions and magnetic fields are closely related. We suggest that the turbulence in the IGM is induced by the cascade of the vorticity generated at cosmological shocks. The turbulence then amplifies the intergalactic magnetic fields (IGMFs) through the stretching of field lines, a process known as the turbulence dynamo. This scenario provides a theoretically motivated model for the evolution of the IGMFs in LSS, independent of the origin of seed fields.

There are other sources that can also provide turbulence and magnetic fields to the IGM. For instance, galactic winds can drag out the galactic magnetic fields on the order of 1 μG strength into the surrounding IGM (*22*). The magnetic fields in the lobes of the jets from galactic black holes can also contaminate the IGM (*23*). Mergers of smaller objects are expected to produce turbulent motions in the ICM, which in turn amplify the existing magnetic fields (*24*). Those processes, although possibly important, are not topics of this study.

We first calculated the vorticity $\vec{\omega} \equiv \vec{\nabla} \times \vec{v}$ (curl of flow velocity) in the IGM, from a numerical simulation using particle-mesh/Eulerian hydrodynamic code (*25*) for the formation of LSS in a cold dark matter–dominated universe with a cosmological constant [supporting online

[1]Department of Astronomy and Space Science, Chungnam National University, Daejeon 305-764, Korea. [2]Department of Earth Sciences, Pusan National University, Pusan 609-735, Korea. [3]Astrophysical Research Center for the Structure and Evolution of the Cosmos, Sejong University, Seoul 143-747, Korea.

*To whom correspondence should be addressed. E-mail: ryu@canopus.cnu.ac.kr

material (SOM) text S1]. As shown in Fig. 1, numerous shocks exist in the LSS that are bounded by accretion shocks (*11*). The distribution of vorticity closely matches that of shocks, suggesting that a substantial portion of the vorticity, if not all, must have been generated at the shocks.

There is a clear trend that the vorticity is larger in hotter (Fig. 2) and denser (fig. S1) regions. As shown in the top right panel of Fig. 2, at the present epoch $\omega_{rms} t_{age} \sim 10$ to 30 (ω_{rms}, the root mean square of the velocity; t_{age}, the present age of the universe) in clusters and groups [temperature (T) > 10^7 K] and filaments ($10^5 < T < 10^7$ K), whereas it is on the order of unity in sheetlike structures ($10^4 < T < 10^5$ K) and even smaller in voids ($T < 10^4$ K) (see SOM text S2 for the temperature phases of the IGM). It increases a little with time and asymptotes after red shift $z \lesssim 1$. Because the local eddy turnover time, t_{eddy}, can be defined with the vorticity as $t_{eddy} = 1/\omega$, $\omega t_{age}(z)$ represents the number of eddy turnovers in the age of the universe at a given z. Roughly, if ωt_{age} is greater than a few, we expect there has been enough time for the vorticity to cascade down to smaller scales and for turbulence to develop in the IGM. So it is likely that turbulence is well developed in clusters, groups, and filaments, but the flow is mostly nonturbulent in sheets and voids.

In our simulation, the vorticity was generated either directly at curved cosmological shocks or by the baroclinity of flows. The baroclinity resulted from the entropy variation induced at shocks. Therefore, the baroclinic vorticity generation also can be attributed to the presence of cosmological shocks. Our estimates of vorticity generation by the two processes (SOM text S3) are shown with open symbols in the top right panel of Fig. 2. They agree reasonably well with the vorticity present in the simulation, although the estimates are intended to be rough. The plot indicates that the contributions from the two processes are comparable.

To estimate the energy associated with turbulence, the curl component of flow motions $\vec{v}_{curl}$, which satisfies the relation $\vec{\nabla} \times \vec{v}_{curl} \equiv \vec{\nabla} \times \vec{v}$, is extracted from the velocity field (SOM text S4). As vorticity cascades to develop into turbulence, the energy $(1/2)\rho v_{curl}^2$ (ρ, gas density) is transferred to turbulent motions, so we regard it as the turbulence energy, ε_{turb}. As shown in Fig. 3, $\varepsilon_{turb} < \varepsilon_{th}$ in clusters and groups. In particular, the mass-averaged value is $\langle \varepsilon_{turb}/\varepsilon_{th} \rangle_{mass} = 0.1$ to 0.3 for $T > 10^7$ K, which is in good agreement with the observationally inferred value in cluster cores (*6*). The turbulence Mach number (M_{turb}) $\equiv v_{turb}/c_s = \sqrt{1.8}(\varepsilon_{turb} / \varepsilon_{th})^{1/2}$, where c_s is the sound speed. Therefore, overall turbulence is subsonic in clusters and groups, whereas it is transonic or mildly supersonic in filaments.

The general consensus regarding the origin of the IGMFs is that no mechanism can produce strong coherent magnetic fields in the IGM before the formation of LSS and galaxies (*26*).

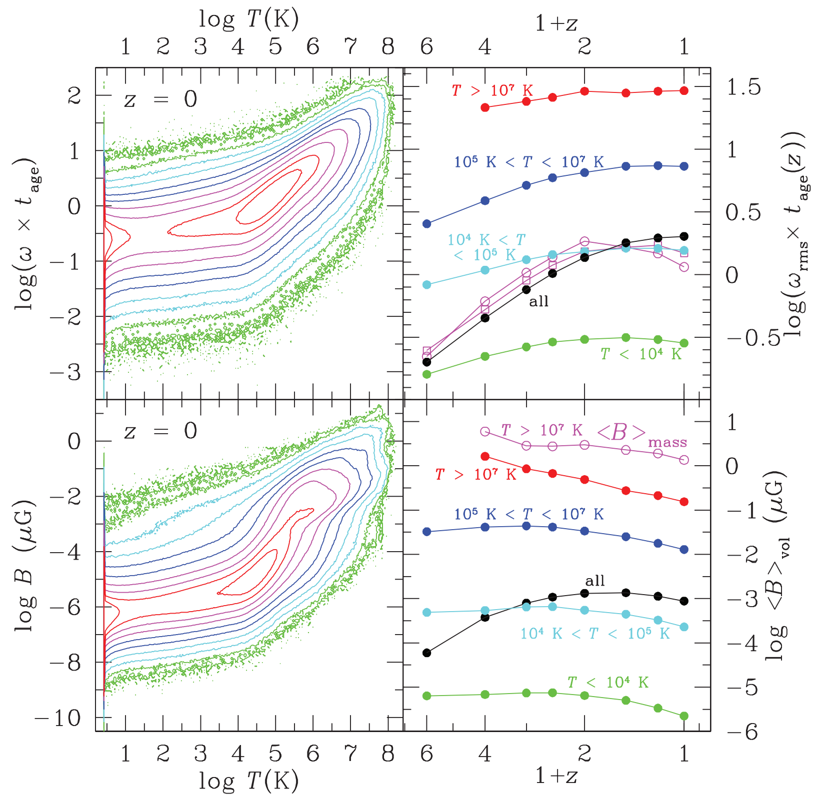

Fig. 2. (**Left**) Volume fraction with given temperature and vorticity magnitude (top left) and temperature and magnetic field strength (bottom left) at present. (**Right**) Time evolution of the root mean square of the vorticity (top right) and volume-averaged magnetic field strength (bottom right) for four temperature phases of the IGM and for all the gas as a function of red shift z. Magenta symbols in the top right panel are our estimates of the vorticity generated directly at curved shocks (open circles) and by the baroclinity of flows (open squares). Magenta open circles in the bottom right panel show the mass-averaged magnetic field strength for $T > 10^7$ K.

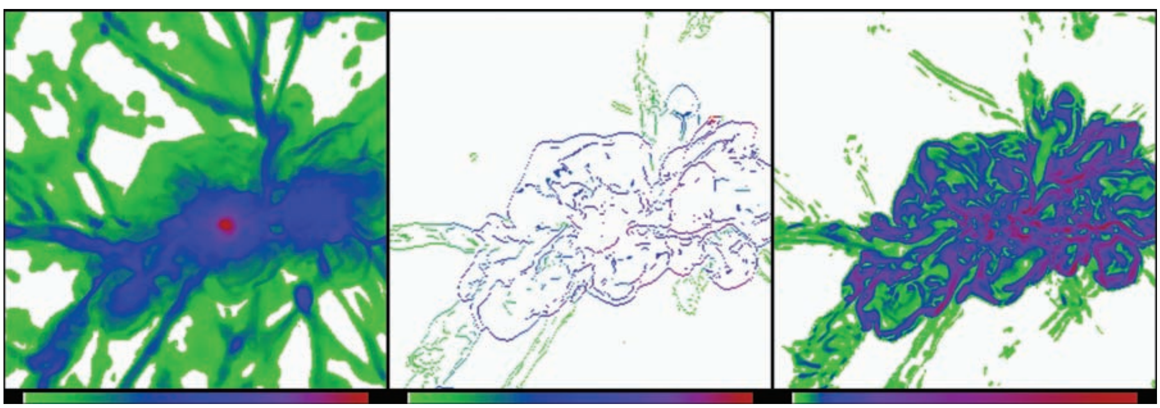

Fig. 1. Two-dimensional images showing gas density ρ in a logarithmic scale (**left**), locations of shocks with color-coded shock speed v_{shock} (**middle**), and magnitude of vorticity, ωt_{age} (**right**), around a cluster complex of (25 h^{-1}Mpc)^2 area at present (z = 0). Here, h is the Hubble constant in units of 100 km s^{-1} Mpc^{-1}. The complex includes a cluster of x-ray emission–weighted temperature $T_x \approx 3.3$ keV. Color codes for each panel are (left) $\rho/\langle\rho\rangle$ from 10^{-1} (green) to 10^4 (red); (middle) v_{shock} from 15 (green) to 1800 km s^{-1} (red); and (right) ωt_{age} from 0.5 (green) to 100 (red).

However, it is reasonable to assume that weak seed fields were created in the early universe (SOM text S5). The seed fields can be amplified by the intergalactic turbulence discussed above. In principle, if we were to perform magnetohydrodynamic (MHD) simulations of structure formation, the amplification of the IGMFs could be followed. In practice, however, the currently available computational resources do not allow a numerical resolution high enough to reproduce the full development of MHD turbulence in LSS (*7*).

In order to follow the growth of the IGMFs by the dynamo action of turbulence, we turned to a separate simulation in a controlled box. Starting with a very weak regular field, a three-dimensional incompressible simulation of driven MHD turbulence was performed (SOM text S6). In the simulation, the evolution of magnetic fields goes through three stages: (i) the initial exponential growth stage, when the back-reaction of magnetic fields is negligible; (ii) the linear growth stage, when the back-reaction starts to operate; and (iii) the final saturation stage (*27*). Adopting the simulation result, we modeled the growth and saturation of magnetic energy as

$$\phi(t/t_{\rm eddy}) = \frac{\varepsilon_B}{\varepsilon_{\rm turb}} = \begin{cases} 0.04 \times \exp[(t/t_{\rm eddy} - 4)/0.36] & \text{for } t/t_{\rm eddy} < 4 \\ (0.36/41) \times (t/t_{\rm eddy} - 4) + 0.04 & \text{for } 4 < t/t_{\rm eddy} < 45 \end{cases} \quad (1)$$

(fig. S2). Assuming that the fraction of turbulence energy governed by Eq. 1, ϕ, is converted into the magnetic energy, we estimate the strength of the IGMFs as $B = [8\pi\varepsilon_{\rm turb} \cdot \phi(\omega t_{\rm age})]^{1/2}$. Here, the values of ω and $\varepsilon_{\rm turb}$ are calculated locally from the structure formation simulation.

The resulting IGMFs follow the cosmic web of matter distribution as shown in Fig. 4 (and in fig. S3). On average, the IGMFs are stronger in hotter (Fig. 2) and denser (fig. S1) regions in our model. The strength of the IGMFs is $B \gtrsim 1$ μG inside clusters and groups (the mass-averaged value for $T > 10^7$ K), ~0.1 μG around clusters and groups (the volume-averaged value for $T > 10^7$ K), and ~10 nG in filaments at present (bottom right panel of Fig. 2) (see SOM text S7 for the numerical convergence of the estimation). These values agree with the observed field strengths discussed earlier. They also agree with the previous study (*7*), in which the magnetic field strength in clusters was estimated to be a fewmicroGauss, based on a kinetic theory. The IGMFs should be much weaker in sheetlike structures and voids. But as noted above, turbulence is not fully developed in such low-density regions, so our model is not adequate to predict the field strength there. For each temperature phase, the IGMFs are stronger in the past, because the gas density is higher. However, the IGMFs averaged over the entire computational volume are weaker in the past because the fraction of strong-field regions is smaller.

While being amplified, magnetic fields become coherent through the inverse cascade (*27*). The coherence scale of magnetic fields in fully developed turbulence is expected to be several times smaller than the driving scale; that is, the scale of dominant eddies (SOM text S8). In the IGM outside of clusters, the curvature radius of typical cosmological shocks is approximately a couple of megaparsecs (*11*) (fig. S4), which should represent a characteristic scale of dominant eddies. The coherence length of the IGMFs there is then expected to be several hundred kiloparsecs. On the other hand, the scale height of the ICM is several 100 kpc. The coherence length in the ICM is expected to be ~100 kpc or so, if it corresponds to the scale of the dominant eddies.

Our model can predict the RMs owing to the IGMFs, which may be tested in future observations with Low Frequency Array and Square Kilometer Array (*28*). Also, our model IGMFs can be employed in the study of the propagation of ultra–high-energy cosmic rays, which is crucial to search for astrophysical accelerators of such high-energy particles (*29*).

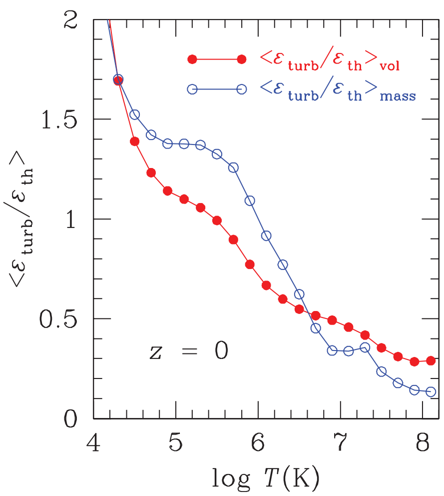

Fig. 3. Ratio of turbulence to thermal energies as a function of temperature at present. The values shown are volume-averaged and mass-averaged over temperature bins.

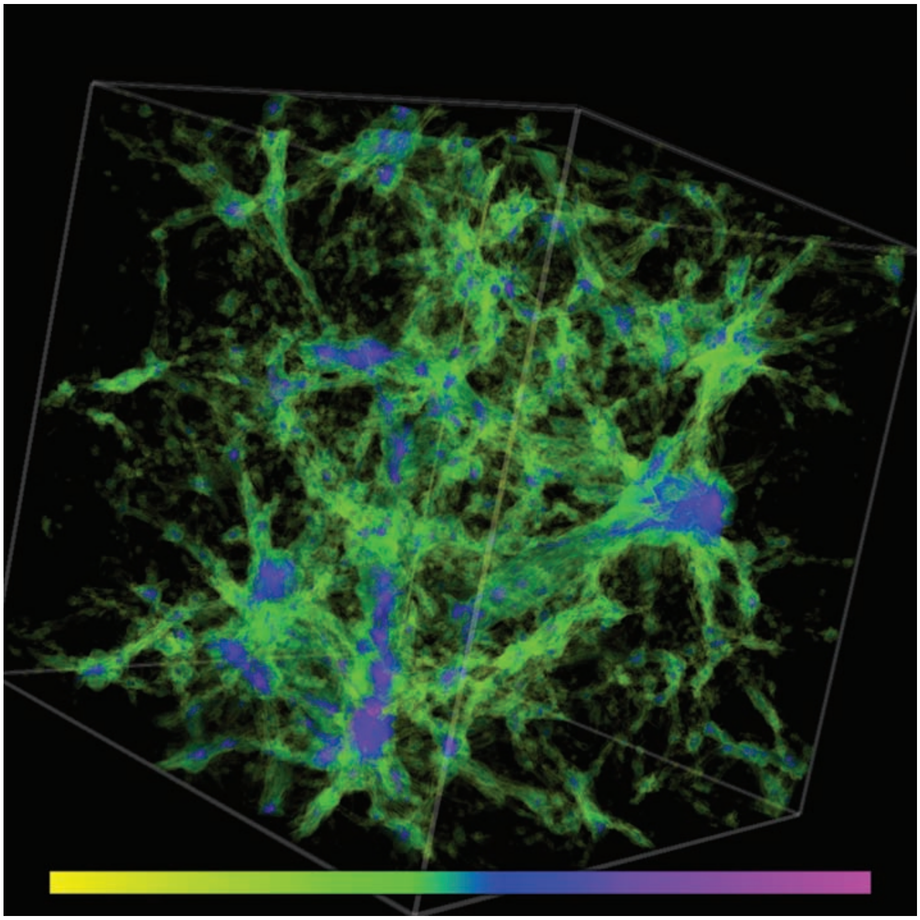

Fig. 4. Volume-rendering image showing the logarithmically scaled magnetic field strength at $z = 0$ in the whole computational box of (100 h^{-1} Mpc)^3 volume. Color codes the magnetic field strength from 0.1 nG (yellow) to 10 μG (magenta). The colors were chosen so that clusters and groups show as magenta and blue and filaments as green.

References and Notes

1. C. L. Carilli, G. B. Taylor, *Annu. Rev. Astron. Astrophys.* **40**, 319 (2002).
2. F. Govoni, L. Feretti, *Int. J. Mod. Phys. D* **13**, 1549 (2004).
3. T. E. Clarke, P. P. Kronberg, H. Böhringer, *Astrophys. J.* **547**, L111 (2001).
4. D. Ryu, H. Kang, P. L. Biermann, *Astron. Astrophys.* **335**, 19 (1998).
5. Y. Xu, P. P. Kronberg, S. Habib, Q. W. Dufton, *Astrophys. J.* **637**, 19 (2006).
6. P. Schuecker, A. Finoguenov, F. Miniati, H. Böhringer, U. G. Briel, *Astron. Astrophys.* **426**, 387 (2004).
7. R. M. Kulsrud, R. Cen, J. P. Ostriker, D. Ryu, *Astrophys. J.* **480**, 481 (1997).
8. D. Nagai, A. Vikhlinin, A. V. Kravtsov, *Astrophys. J.* **655**, 98 (2007).
9. M. Murgia *et al.*, *Astron. Astrophys.* **424**, 429 (2004).
10. C. Vogt, T. Enßlin, *Astron. Astrophys.* **434**, 67 (2005).
11. D. Ryu, H. Kang, E. Hallman, T. W. Jones, *Astrophys. J.* **593**, 599 (2003).
12. C. Pfrommer, V. Springel, T. A. Enßlin, M. Jubelgas, *Mon. Not. R. Astron. Soc.* **367**, 113 (2006).
13. H. Kang, D. Ryu, R. Cen, J. P. Ostriker, *Astrophys. J.* **669**, 729 (2007).
14. K. B. Quest, *J. Geophys. Res.* **93**, 9649 (1988).
15. A. R. Bell, *Mon. Not. R. Astron. Soc.* **182**, 147 (1978).
16. R. D. Blandford, J. P. Ostriker, *Astrophys. J.* **221**, L29 (1978).
17. L. Biermann, *Z. Naturforsch.* **5a**, 65 (1950).
18. E. S. Weibel, *Phys. Rev. Lett.* **2**, 83 (1959).
19. M. V. Medvedev, L. O. Silva, M. Kamionkowski, *Astrophys. J.* **642**, L1 (2006).
20. J. Binney, *Mon. Not. R. Astron. Soc.* **168**, 73 (1974).
21. G. Davies, L. M. Widrow, *Astrophys. J.* **540**, 755 (2000).
22. H. J. Völk, A. M. Atoyan, *Astropart. Phys.* **11**, 73 (1999).
23. P. P. Kronberg, Q. W. Dufton, H. Li, S. A. Colgate, *Astrophys. J.* **560**, 178 (2001).
24. K. Subramanian, K. A. Shukurov, N. E. L. Haugen. *Mon. Not. R. Astron. Soc.* **366**, 1437 (2006).
25. D. Ryu, J. P. Ostriker, H. Kang, R. Cen, *Astrophys. J.* **414**, 1 (1993).
26. R. M. Kulsrud, E. G. Zweibel, *Rep. Prog. Phys.* **71**, 046901 (2008).
27. J. Cho, E. T. Vishniac, *Astrophys. J.* **538**, 217 (2000).
28. B. M. Gaensler, R. Beck, L. Feretti, *N. Astron. Rev.* **48**, 1003 (2004).
29. S. Das, H. Kang, D. Ryu, J. Cho, *Astrophys. J.* **681**, in press (2008).

30. This work was supported by the Korea Foundation for International Cooperation of Science and Technology through grant K20702020016-07E0200-01610 provided by the Ministry of Education, Science and Technology. The work of D.R. was also supported by the Korea Science and Engineering Foundation (KOSEF) through the grant of basic research program R01-2007-000-20196-0. The work of H.K. and S.D. was also supported by KOSEF through the Astrophysical Research Center for the Structure and Evolution of the Cosmos. The work of J.C. was also supported by the Korea Research Foundation, grant KRF-2006-331-C00136, funded by the Korean Government.

Supporting Online Material

www.sciencemag.org/cgi/content/full/320/5878/909/DC1
Materials and Methods
SOM Text
Figs. S1 to S6
References

7 January 2008; accepted 10 April 2008
10.1126/science.1154923

Stress and Fold Localization in Thin Elastic Membranes

Luka Pocivavsek,[1] Robert Dellsy,[2] Andrew Kern,[1] Sebastián Johnson,[3] Binhua Lin,[2] Ka Yee C. Lee,[1] Enrique Cerda[3]*

Thin elastic membranes supported on a much softer elastic solid or a fluid deviate from their flat geometries upon compression. We demonstrate that periodic wrinkling is only one possible solution for such strained membranes. Folds, which involve highly localized curvature, appear whenever the membrane is compressed beyond a third of its initial wrinkle wavelength. Eventually the surface transforms into a symmetry-broken state with flat regions of membrane coexisting with locally folded points, reminiscent of a crumpled, unsupported membrane. We provide general scaling laws for the wrinkled and folded states and proved the transition with numerical and experimental supported membranes. Our work provides insight into the interfacial stability of such diverse systems as biological membranes such as lung surfactant and nanoparticle thin films.

Crumple a piece of paper and a meshwork of highly deformed ridges and perfectly straight planes appear. This focusing behavior is universal for any strongly confined membrane (*1*, *2*). Compress a similar membrane now resting on some substrate like water or a gel, and it responds differently. Its initial response is wrinkling, producing beautiful sinusoidal undulations across the entire surface (*3*–*7*). Yet if the wrinkled surface is laterally compressed even further, a different geometry emerges. The wrinkles disappear everywhere except for a few select locations on the surface that exhibit folds, a geometry similar to the crumpled piece of paper.

A variety of real systems can be thought of as elastic membranes resting on softer substrates. Our lungs are lined by a thin membrane, composed of lipids and proteins, that stabilizes them and is often modeled as an elastic sheet on a fluid subphase (*8*–*10*). The membrane's mechanical response via reversible folding is believed to play a key role in normal lung function (*9*). Likewise, thin layers of nanoparticles—which show promise as unique electronic, optical, and magnetic materials (*11*)—have recently been spread at air/water interfaces as a method of controlling their packing structure and to allow ease of deposition onto solid substrates for potential technological use (*12*, *13*). Wrinkling and folding of such layers during deposition could be exploited to create nanopatterned structures.

Several theoretical approaches have been developed to treat particular cases of either wrinkling (*3*, *6*, *7*, *14*–*16*) or folding (*8*, *17*, *18*) in given systems. However, the generality of these instabilities has not been developed, and existing theories treat one state or the other without connecting the two. Here, we explore the evolution of a general elastic interface under lateral compression. We show that wrinkles appear as a first-order linear response of the membrane and can be suppressed by nonlinear effects that give rise to the fold at greater confinement.

A thin (10-μm) sheet of polyester resting on the surface of water is initially flat. Clamping one set of free edges between two movable barriers and compressing by some small amount Δ, the sheet instantaneously forms wrinkles with a wavelength λ (a in Fig. 1A). If the sheet is continually compressed, the wrinkle amplitude grows uniformly across the surface (*19*). Eventually one wrinkle will grow in amplitude, whereas the others decay as seen in b in Fig. 1A. Further confinement leads to the eventual formation of a fold where all of the distortion is focused within a narrow region of the surface (c in Fig. 1A).

Although the wrinkle-to-fold transition in Fig. 1A takes place when the polyester sheet is lying on top of water, a fluid substrate is not necessary for the transition. Figure 1B shows a similar evolution of the surface with the polyester adhered to a soft gel. Smooth wrinkling (a in Fig. 1B) becomes unstable (b in Fig. 1B) and eventually localizes into several folds relaxing the rest of the surface (c in Fig. 1B).

A phenomenologically similar transition can be observed in films three orders of magnitude thinner. At an air/water interface, gold nanoparticles 5 nm in diameter are compressed to form a self-assembled trilayered film that is 15 nm thick. With the use of light microscopy, one can observe the initial periodic wrinkles with λ ~ 10 μm (a in Fig. 1C). If the compression is stopped, the surface remains wrinkled. However, further confinement leads to the focusing behavior observed in the macroscopic polyester film. Panel b in Fig. 1C shows the beginning of fold formation: The brightness of one wrinkle increases as its amplitude grows, scattering more light. Eventually the two leaflets of the sheet make self-contact, and the fold

[1]Department of Chemistry and James Franck Institute (JFI), University of Chicago, Chicago, IL 60637, USA. [2]Center for Advanced Radiation Sources and JFI, University of Chicago, Chicago, IL 60637, USA. [3]Departamento de Física and Centro para Investigación Interdisciplinaria Avanzada en Ciencias de los Materiales, Universidad de Santiago, Av. Ecuador 3493, Santiago, Chile.

*To whom correspondence should be addressed. E-mail: ecerda@lauca.usach.cl

Turbulence and Magnetic Fields in the Large-Scale Structure of the Universe

Dongsu Ryu, Hyesung Kang, Jungyeon Cho and Santabrata Das

Science **320** (5878), 909-912.
DOI: 10.1126/science.1154923